

Analysis of Dynamic Loads on Azimuthing Ducted Propulsor under Off-Design Operation Conditions

Nabila Berchiche¹, Vladimir Krasilnikov¹, Kouros Koushan¹

¹ SINTEF Ocean, Trondheim, Norway

ABSTRACT

In the present study, the results of CFD simulations by the unsteady RANS method of the flow around a generic model of azimuthing ducted pushing thruster are presented and compared with the results of model tests. The calculations are performed with the propeller operating at the design pitch ($P_{0.7}/D=1.1$) for different advance coefficients in straight and oblique flow conditions. The main quantities considered in the validation study include propeller thrust and torque, duct thrust and side force, total thrust and total side force as well as the thruster steering moment. In addition, the loads acting on a single propeller blade are also compared to the experimental data. A good agreement between the calculations and measurements is achieved for most quantities except the steering moment that shows larger relative differences from the measured values. However, the overall variation of the steering moment with loading and heading angle appears to be qualitatively captured by the numerical simulations. Separately, CFD simulations are performed with the same thruster operating in presence of initially undisturbed free surface, at different magnitudes of submergence, in order to illustrate the impact on propulsor forces and individual blade loads.

Keywords

CFD, RANS, Ducted pushing podded thruster, Oblique flow, Unsteady loads.

1 INTRODUCTION

The ducted azimuthing propulsors have become a very popular solution for propulsion system on such vessels as tugboats, anchor handlers, offshore supply vessels, research vessels and others. They are found to combine the advantages of ducted propellers under heavy loading operation conditions with superior maneuvering characteristics of pod propulsors at low speed operation, while offering reasonable efficiency at free sailing. At the same time, azimuthing propulsors may experience considerable deterioration of their performance characteristics and come at risk of failure due to high dynamic loads arising from various factors. Heavy propeller loading in combination with large azimuth angles is the frequent scenario at low speed operation that results

in unsteady loads of high amplitude on the whole propulsor as well as on the individual propeller blades. These loads put extra demands on structural strength of propulsor, and reliability of blade bearings and transmission mechanisms. The operation conditions are further complicated by vessel drift, presence of sea current, orbital velocities induced by free surface waves, and wave induced ship motions. Massive flow separation develops on propulsor components such as pod housing and duct, and it makes the inflow on a pushing propeller highly inhomogeneous. As a consequence, propeller blades may experience sheet and vortex cavitation of unsteady nature, causing increased levels of noise and vibration, and posing danger of blade erosion. Operation in the vicinity of free surface poses a great risk of ventilation when propeller loading is heavy. The aforementioned aspects of propulsor operation are in the focus of the ongoing R&D Project "INTER-THRUST" supported by the MARTEC II ERA-NET program (Maritime Technologies), where the authors participate on behalf of SINTEF Ocean (formerly, MARINTEK)

The complexity of hydrodynamic interactions taking place between the components of a ducted azimuthing propulsor has been noted by many authors (Funeno, 2009; Palm et al, 2011), and it calls for advanced numerical methods, such as those of CFD (Computational Fluid Dynamics), when one should target improvements in propulsor design and its operational reliability. For the successful implementation of CFD results in design practice, validation is however crucial. While there is a considerable amount of validation material for pod propulsors with open propellers, for ducted podded units the available data are limited. In the present work, the authors attempt a detailed validation study with a generic model of the ducted pod unit tested at SINTEF Ocean facilities. The comparisons between the numerical simulations and experiments cover the range of operation conditions from bollard to free sailing, and a wide range of heading angle at fixed propeller RPM and zero pivoting speed. Both the total forces and moments acting on the unit and loads on single blade are investigated. Separately, CFD simulations are performed with the same thruster operating in presence of initially undisturbed free surface, at different magnitudes of submergence, in order to illustrate the impact on propulsor forces and individual blade loads.

2 PROPULSOR MODEL CHARACTERISTICS AND SIMULATED CONDITIONS

The main characteristics of the generic model of the azimuthing ducted pushing thruster tested in the towing tank at SINTEF Ocean (formerly, MARINTEK) and used in the CFD simulations are given in Table 1. A more detailed model specification, including propeller blade drawings, is found in (Koushan, 2006a). Regarding the propeller model, it has to be noted that the blade design represents a compromise solution between an open propeller and a ducted propeller, since the same propeller model and the same pod unit has earlier been tested in both the ducted and open configurations (Koushan, 2007; Koushan & Krasilnikov, 2008). The model tests are conducted at constant propeller shaft immersion of 345 mm ($1.38D_p$, where D_p is the propeller diameter). A plate is mounted on top of the thruster to avoid wave generation and aeration. Still, at high heading angles propeller rate of revolution had to be reduced, in order to avoid aeration and mitigate excessive free surface disturbance. The propeller was driven by an electric motor installed on top of the thruster via a right-angle transmission gear. A six-component balance was positioned on top of the thruster unit to measure total loads on the thruster, including propeller, but excluding the duct. A cylindrical rod of 35 mm diameter connected the duct to the two force transducers, which measured separately the axial and transverse forces acting on the duct. A propeller balance measured propeller thrust and torque, the measured signals being wirelessly transmitted to the acquisition system. During the blade loads measurements, one of the propeller blades was mounted on a blade dynamometer placed inside the hub. A pulse meter on the shaft provided propeller rate revolutions, while another pulse meter inside the thruster registered the angular position of reference blade. An angular meter was installed on top of the rig to measure the heading angle of the unit. A picture of test set-up is presented in Figure 1. The tests are performed at different heading angles ranging from -90 degrees to +90 degrees, at both negative and positive advance coefficients. The measured forces and moments include propeller thrust and torque, duct thrust and side force, total thrust and total side force, steering moment, blade thrust and torque, and blade spindle and bending moments.

The conditions selected for the validation studies are summarized in Table 2. In addition, the bollard pull condition ($J=0.0$) has been also simulated. The thrust force, F_x , is defined along the propeller shaft axis, and is positive forward. The side force, F_z , is the horizontal force perpendicular to propeller shaft axis, and is positive to portside. The steering moment, M_y , is positive in anti-clockwise direction when viewing from above. Positive heading angles correspond to crossflow from portside.



Figure 1. Test set-up

Table 1. Characteristics of MARINTEK Propulsor model

Model thruster:	
Vertical distance from propeller centre to top of the housing [mm]	42
Total length of housing [mm]	181
Length of parallel section of the strut [mm]	86
Model Propeller P-1374 (Right-handed):	
Propeller diameter [mm]	250
Hub diameter [mm]	60
Design pitch ratio $P_{0.7}/D$	1.1
Skew [degrees]	25
Expanded blade area ratio	0.6
Number of blades	4
Model duct (19A type):	
Length [mm]	125
Inner diameter [mm]	252.78
Max. outer diameter [mm]	303.96
Leading edge radius [mm]	2.78
Trailing edge radius [mm]	1.39

Table 2. Simulated Conditions

Advance Coefficient J	Heading angle [deg]
0.6 (near max efficiency)	$\pm 60, \pm 35, \pm 15, 0$
0.3	$\pm 35, \pm 15, 0$

3 NUMERICAL SET-UP

3.1 CFD Method

Unsteady RANS (Reynolds-Averaged Navier-Stokes) equations are solved in the commercial solver STAR-CCM+ (Version 11.02.010), using a finite volume method, to simulate the flow around a ducted pushing thruster. The simulations are carried out using a sliding mesh technique, which allows the mesh region that contains propeller to rotate at the same rotational speed as that of propeller with respect to the outer region of stationary fluid. The implicit unsteady model is used with a first-order temporal discretization scheme. The flow is considered fully turbulent, and turbulence effects are modelled with the

Shear-Stress-Transport (SST) $k-\omega$ model in most of simulations, except additional test calculations in straight flow condition, which have been done with the GaReTheta transition model, based on the same SST $k-\omega$ model formulation. The turbulence models are used in combination with all- y^+ wall treatment.

3.2 Computational domain and Mesh

The computational domain consists of two sub-domains (mesh regions): a rotating sub-domain that contains the propeller and a stationary sub-domain that includes the gondola, strut, and part of the duct and hub. The inlet and outlet of computation domain are placed at 22 propeller diameter (D_p) from the propeller center, and sides boundaries are placed at $10 D_p$. The rotating sub-domain is a cylinder surrounding the propeller. Both its upstream and downstream boundaries are located at $0.15 D_p$, and the radial boundary is located at approximately $0.53 D_p$ from the propeller center, as shown in Figure 2. Note that the radial boundary of the rotating propeller domain coincides with inner surface of the duct. Therefore, only two sliding interfaces are defined between the stationary and rotating regions as illustrated in Figure 2.

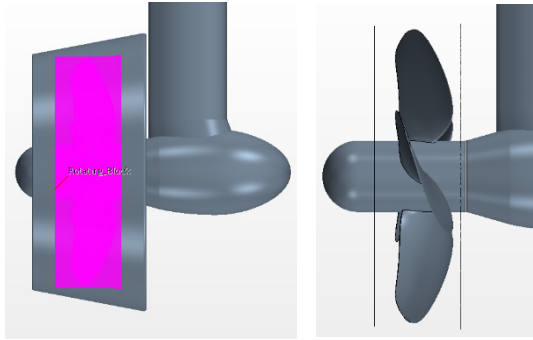


Figure 2. View of the propeller rotating region (left) and location of the sliding interfaces (right).

The computational grid is generated in STAR-CCM+ using polyhedral cells in the rotating mesh block and hexahedral trimmed cells in the stationary mesh block. The boundary layer mesh consists of 10 prismatic layers applied on all solid surfaces, except on the extended part of the strut. The values of the stretching factor and total thickness of the boundary layer has been set in order to have a range of y^+ of $[0\div 5]$ in model scale calculations, and at the same time ensure sufficiently smooth transition from the boundary layer mesh to the core mesh

The total grid size is approximately 21.44 million cells, with 4.03 million cells located inside the propeller block. Figure 3 to Figure 5 show some views of the surface mesh on the duct, blades and pod, and on the vertical plane cutting through the propeller center.

The boundary conditions are as follows: a uniform inlet velocity assigned at the inlet; a pressure outlet at the outlet boundary; a velocity inlet at the remaining sides of the domain; and a no-slip wall condition is set on all solid surfaces except the extended part of the strut where a slip wall condition is applied.

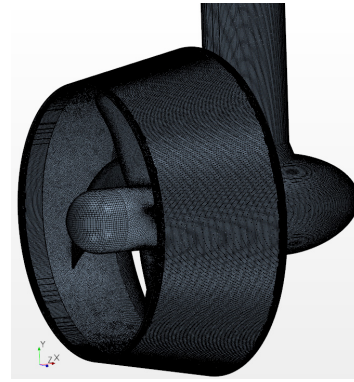


Figure 3. Surface mesh on the duct.



Figure 4. Surface mesh on the duct and pod.

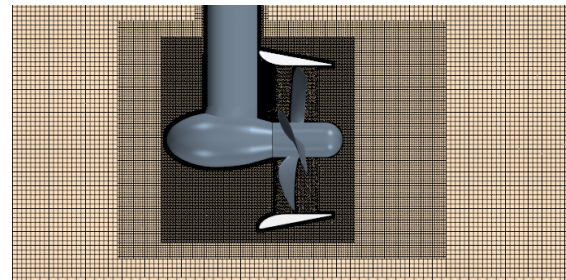


Figure 5. View of the mesh on a vertical plane.

4 RESULTS AND MODEL-SCALE VALIDATION

All the simulations are run for 40 propeller revolutions with a time-step corresponding to 1 degree of propeller rotation, and propeller rps set to 11 Hz. For comparison with measurements, the forces and moments are expressed as non-dimensional coefficients by dividing them by $(\rho n^2 D^4)$ and $(\rho n^2 D^5)$, respectively. In the simulations, the force and moment coefficients are time-averaged over the last 20 propeller revolutions.

4.1 Integral forces and moments on propulsor

The computed and measured propeller thrust KTP , propeller torque KQP , duct thrust KTD and total unit thrust force $KTTOT$ are illustrated in Figure 6 and Figure 7. The numerical simulations appear to under-predict the propeller thrust for most cases. However, the overall variation of KTP with the heading-angle is well captured for all loadings. The propeller torque KQP is better predicted than KTP for most of tested conditions. At

heavier loading ($J=0.3$), KQP is in a very good agreement with the measurements for the whole range of heading angles. At $J=0.6$, the computed KQP values are also close to the measured data except the large heading angles, where an over-prediction is observed. The latter scenarios are associated with massively separated flow over the pod and duct, and therefore represent considerable challenges in numerical simulations.

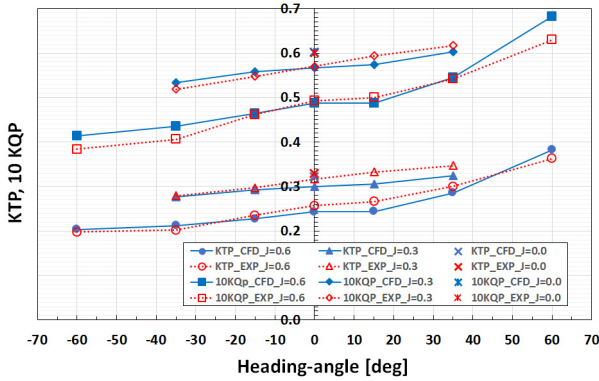


Figure 6. Measured and calculated propeller thrust and torque at different loadings and heading-angles.

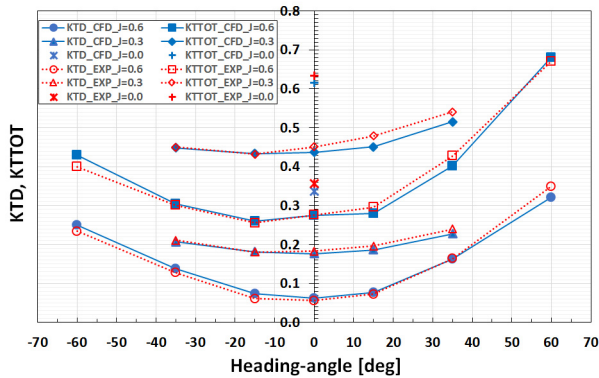


Figure 7. Measured and calculated duct thrust KTD and total thrust KTTOT at different loadings and heading-angles.

Regarding the under-prediction of KTP, at least two important phenomena are believed to play a role: effect of the gap between the rotating hub and stationary pod, and effect of the flow over the duct.

The first phenomenon is related to the gap effect. For this propulsor, CFD calculations in straight flow are performed for different loadings and two pitch ratios. The simulations predict lower pod resistance (KTG) and lower KTP, compared to the measurements, while the computed total thrust KTTOT is predicted closely to the measured data. This has been observed for the whole range of tested conditions (all loadings and P/D), see Figure 8. In the CFD model, the gap width is included in exact accordance with

the test setup, however all details of shafting, bearings and seals are not modelled. Furthermore, there are also uncertainties associated with the pressure levels in the gap during model tests and their effect on the measured propeller thrust KTP. The second phenomenon is attributed to the flow over the duct at low Re numbers in model scale, and it is associated with flow transition, especially on the outer side of the duct. Unlike the former phenomenon (gap effect), it is mostly evident at light loading conditions.

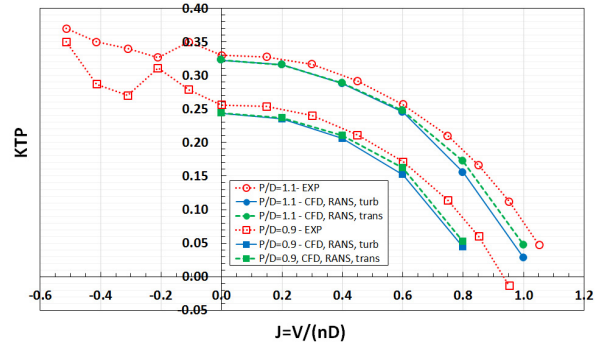


Figure 8. Results of straight flow condition at different loadings: measured and computed KTP.

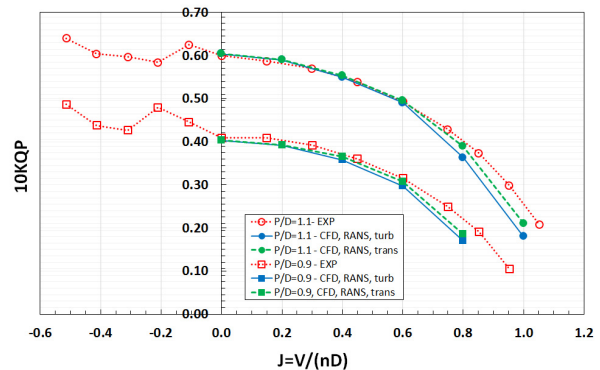


Figure 9. Results of straight flow condition at different loadings: measured and computed KQP.

Flow transition affects the extent of flow separation on the duct and also the flow pattern over the duct trailing-edge (T.E). It is mainly the second effect (T.E. flow) that influences the flow velocity through the duct and results in changes in propeller KTP and KQP. In most cases, for conventional shaft ducted propellers, it has been observed that transition leads to a somewhat larger expansion rates of propeller slipstream and hence lower velocity through the propeller compared to the fully turbulent conditions (Bhattacharyya et al, 2016). This results in an increase of propeller thrust and torque as observed in Figure 8 and Figure 9, where the results of calculation in fully turbulent flow are compared with the results obtained using the transition model. For heavier loading conditions ($J \leq 0.6$), in straight flow, propeller torque KQP is very well predicted, while at lighter loading conditions ($J > 0.6$), KQP

is under-predicted as it can be seen from Figure 9. Since propeller torque is not influenced by the gap flow effect, one can conclude that in the range of loadings $J \leq 0.6$, the influence of flow transition is minor, and the main reason for the differences in KTP prediction should probably be attributed to uncertainties associated with gap flow in both the physical and numerical models. In oblique flows, the flow around the gap is not any longer axisymmetric, and per consequent, the contributions of gap walls to pod resistance and propeller thrust change. In such cases, the gap flow is also strongly influenced by configurations of hub and pod in the vicinity of the gap, and vortices shed from the housing. Therefore, in the case of oblique flows, even small difference in flow pattern between the simulations and tests may result in quite large differences in contributions to thrust from the gap walls.

Figure 6 shows that propeller thrust and torque increase with the increase of positive heading angle, while they decrease with the increase of negative heading angle, in comparison with their values at zero heading. This asymmetry of forces with respect to zero heading is a characteristic feature of pushing podded units, and it is mainly associated with the interaction of the rotating propeller with the cross-flow in separated wake behind the strut. This phenomenon has been discussed in details by Krasilnikov et al (2009). For ducted pushing propulsors, the asymmetry is smaller than for open pushing propulsors, due to the flow-straightening effect of the duct. Furthermore, as observed on Figure 6, the asymmetric influence of cross-flow altered by the strut wake on KTP is larger for lighter loadings.

The predictions of duct thrust and total thrust forces on the unit compare quite well to the measurements. As seen on Figure 7, KTD exhibits a symmetry with respect to zero heading angle, since the duct experiences very similar conditions in terms of inflow and strut wake at positive and negative headings. Most of asymmetry in KTD observed at large heading angles is due to the asymmetry of propeller thrust.

Comparison of measured and computed duct side force, total side force and steering moment are presented in Figure 10, Figure 11 and Figure 12, respectively. The major contribution to the side force comes from the duct at all headings, and as the heading angle increases, the contributions from the pod and propeller are added. It has to be noted that due to the flow straightening effect of the duct on propeller flow, the contribution of propeller to the total side force is much smaller than it is in the case of open pushing thrusters. The duct straightens both the oblique inflow onto propeller and the slipstream downstream of the propeller. These two effects result in a reduction of propeller side force.

The numerical simulations appear to under-predict the total side force for all tested conditions. This is obviously due to the under-prediction of the duct side force (KSD). It has been concluded from earlier studies on the cases where flow separation develops on the duct in straight flow that a

fully turbulent calculation results in a greater separation extent than obtained from the calculation using the transition model (Bhattacharyya et al, 2016). Hence, the under-prediction of KSD may be attributed to an over-prediction of flow separation on the duct, which leads to a reduction of the lift force.

The calculated steering moment KMY (excluding duct contribution) is compared to the experimental data in Figure 12.

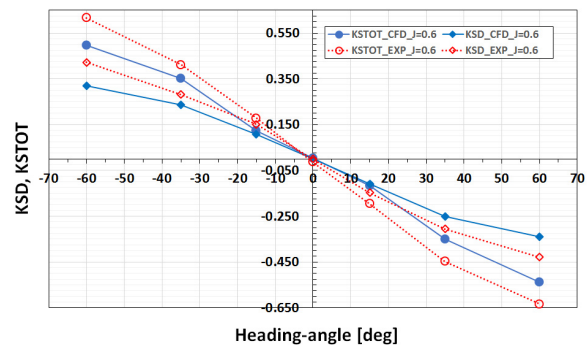


Figure 10. Measured and calculated duct side force KSD and total side force KSTOT at $J=0.6$ for different heading angles.

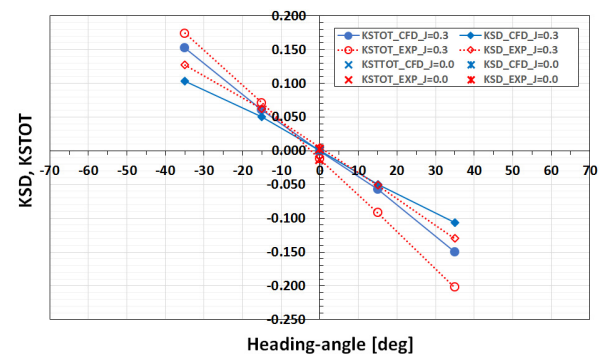


Figure 11. Measured and calculated duct side force KSD and total side force KSTOT at bollard pull condition and at $J=0.3$ for different heading angles.

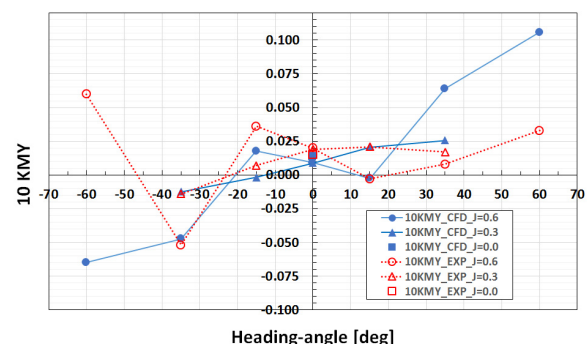


Figure 12. Measured and calculated steering moment KMY (excluding duct contribution) at different loadings and heading angles.

Large deviations are observed between the measurements and the numerical predictions, particularly at high advance coefficient and at large heading angles. However, the overall variation of the steering moment with the loading and heading angle appears qualitatively well reproduced by the CFD simulations. The quantitative agreement is more difficult to achieve, since the values of KMY are small, because KMY is the result of opposing contributions from propeller (KMY_P) and pod (KMY_G). At zero heading, KMY is entirely determined by the contribution from propeller. Minor difference in the location of resulting

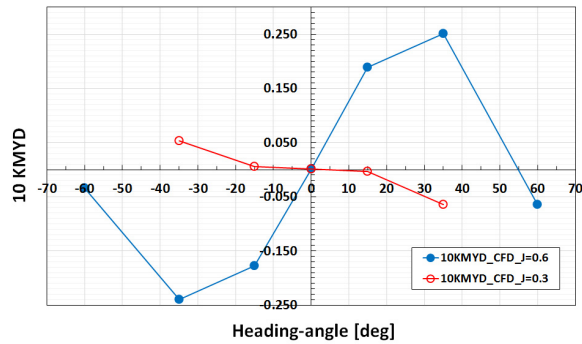


Figure 13. Calculated steering moment of the duct KMYD at different loadings and heading-angles.

force centers on the pod and propeller may lead to considerable difference in contributions of the respective forces to KMY due to the force arm. Both the side force on propeller (KSP) and side force on pod (KSG) act in the direction of cross-flow caused by the heading angle. At zero heading, propeller develops a small side force acting in the direction of portside (for right-handed propeller) due to its interaction with the wake of the pod housing. This small side force causes a deviation of the total reaction force, resulting in a non-zero positive steering moment acting on the unit. The KMY moment is larger at lower J values, where propeller loading is heavier. This is an important phenomenon that has direct impact on course-keeping characteristics of vessels equipped with pushing and dual-end pod propulsors.

At heading angles, the major contribution to the total steering moment (KMY_{TOT}) comes from the duct. It can be observed from Figure 13 that, for the same heading angle, the steering moment of the duct (KMYD) may be of different sign, depending on loading condition. More specifically, for the positive heading angle of +35 degrees, at J=0.6 the moment KMYD is positive, i.e. it tends to turn the rear part of the unit in the direction of cross-flow (opposite clockwise), whereas at J=0.3 KMYD acts in opposite direction. This result is explained by the differences in contribution to KMYD originating from the duct thrust and duct side force at different loading conditions. The side force developed on the duct tends to turn the rear part of the unit in the direction of cross-flow, similar to the side force on propeller. The force center of the duct reaction in oblique flow is however not located at

the propeller shaft, but is shifted towards the windward side of the duct (side facing the cross-flow), and thus the duct thrust tends to turn the rear part of the unit in the direction opposite to cross-flow. At lighter loading conditions (J=0.6), the duct side force gives a greater contribution to KMYD. At heavier loading conditions (J=0.3), it is on the contrary the duct thrust that gives a greater contribution to KMYD, which explains the differences observed in the results. As the heading angle increases, a massive flow separation develops on the duct at higher speeds (J=0.6). It slows down the growth of duct side force with heading angle, while duct thrust continues to increase with approximately the same gradient as at lower heading angles. Thus, the ratio KSD/KTD is reduced, and due to the redistribution of pressure on the duct, the arm of the KSD contribution is reduced as well. These changes result in a rapid decrease of the steering moment produced by the duct.

Separately, a frequency analysis is performed using the Fast Fourier Transform (FFT) on the computed time histories of propulsor forces and moments. This analysis captured in addition to the propeller blade frequency of 44Hz, a lower frequency peak in the range of 3.9÷4.2Hz, as shown in Figure 14 for duct thrust. This low frequency is found to be related to the vortex shedding process that accompanies flow separation on the leeward side of the duct. Because of the interaction the low frequency peaks in the same range are also observed for loads on other propulsor components.

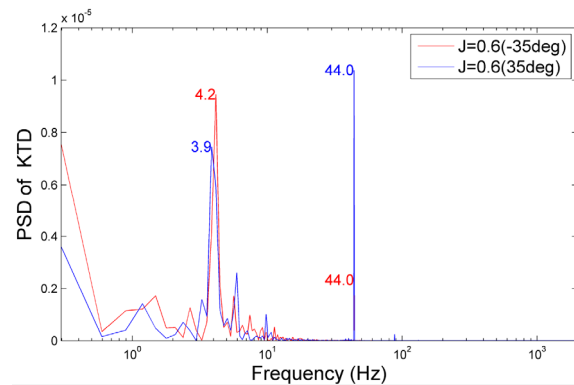


Figure 14. Power spectral density of duct thrust at J=0.6 for the positive and negative heading angles of 35 degrees.

4.2 Blade Loads

The computed and measured time-averaged values of the non-dimensional blade thrust KT_b , blade torque KQ_b , spindle moment KMY_b and bending moment KMZ_b coefficients and their corresponding standard deviation values are summarized in Table 3 for J=0.6 and in Table 4 for J=0.3. The standard deviations values (σ) are expressed as a percentage of the mean values. The origin of blade-fixed coordinates system is set at the blade root as defined

in model tests. The bending moment is positive when it bends the blade in the direction from pod to hub (from upstream to downstream), and the spindle moment is positive in clockwise direction when viewed from blade tip. The predictions compare quite well to the experimental data especially regarding the blade thrust. The values of spindle moment are very small and therefore sensitive to small variations. The computed fluctuations are close to the measured values and, as expected, they increase as the magnitude of the heading angle increases.

Table 3. Measured and computed blade forces and moments at J=0.6 for different heading angles.

Variable	-35 deg		-15 deg		0 deg		15 deg		35 deg	
	CFD	EXP	CFD	EXP	CFD	EXP	CFD	EXP	CFD	EXP
KTb	0.055	0.049	0.058	0.056	0.062	0.059	0.061	0.063	0.071	0.071
$\sigma(KTb)(\%)$	36.4	38.9	16.8	17.5	5.8	6.3	11.6	13.1	22.1	22.0
10KQb	0.071	0.086	0.075	0.089	0.079	0.098	0.078	0.095	0.087	0.087
$\sigma(KQb)(\%)$	24.8	23.5	12.3	12.1	4.2	4.8	8.0	8.5	15.1	19.0
10KMYb	0.021	0.016	0.021	0.015	0.019	0.008	0.020	0.011	0.016	0.012
$\sigma(KMYb)(\%)$	126.3	194.4	51.2	95.7	20.6	64.9	53.6	100.1	157.6	247.0
10KMZb	-0.130	-0.117	-0.136	-0.152	-0.143	-0.171	-0.140	-0.170	-0.158	-0.180
$\sigma(KMZb)(\%)$	26.5	35.4	13.4	15.6	4.6	4.6	8.5	10.0	15.7	17.5

Table 4. Measured and computed blade forces and moments at J=0.3 for different heading angles.

Variable	-35 deg		-15 deg		0 deg		15 deg		35 deg	
	CFD	EXP	CFD	EXP	CFD	EXP	CFD	EXP	CFD	EXP
KTb	0.071	0.070	0.074	0.075	0.076	0.071	0.077	0.078	0.081	0.079
$\sigma(KTb)(\%)$	11.9	12.0	7.1	8.0	4.0	4.7	5.3	6.6	8.1	10.8
10KQb	0.087	0.099	0.091	0.096	0.092	0.112	0.093	0.108	0.097	0.101
$\sigma(KQb)(\%)$	8.3	9.8	5.4	6.9	3.0	3.6	3.7	4.9	5.3	9.3
10KMYb	0.014	0.008	0.012	0.001	0.012	-0.006	0.011	-0.004	0.010	0.000
$\sigma(KMYb)(\%)$	80.8	165.2	52.1	689.6	29.2	48.4	52.4	106.2	105.9	3776.1
10KMZb	-0.167	-0.176	-0.173	-0.198	-0.175	-0.205	-0.177	-0.206	-0.185	-0.222
$\sigma(KMZb)(\%)$	8.6	9.5	5.8	6.4	3.4	3.5	4.1	5.3	5.8	8.4

The examples of computed time histories of blade thrust and bending moment are shown in Figure 15 and Figure 16 for the two heading angles (± 35 degrees) at J=0.6. The measured values are also plotted for comparison. The horizontal lines represent the time-averaged values and the vertical lines represent the 12 o'clock positions of the reference blade. A good agreement is observed between the calculations and measurements, particularly for KTb. Similar observations are made for all tested conditions. Figure 17 illustrates contours of the axial velocity together with the tangential velocity vectors on a control plane upstream the propeller for the positive and negative heading angles of 35 degrees.

It is seen from the time-histories of KTb and Figure 17 how the inflow on propeller generated by the interaction of the cross-flow and strut wake, results in mentioned KTP asymmetry for pushing propellers. At positive heading angles, the blade of a right-handed pushing propeller will experience heaviest loads at 6 o'clock position, where it encounters the cross-flow induced by the heading angle,

see Figure 17. Around 12 o'clock position, the same cross-flow would result in a decrease of blade loads, but the separated wake from the strut produces velocities opposite to the cross-flow, which increases the blade loading. Two peaks are observed in the time-histories of KTb at positive heading, see Figure 15.

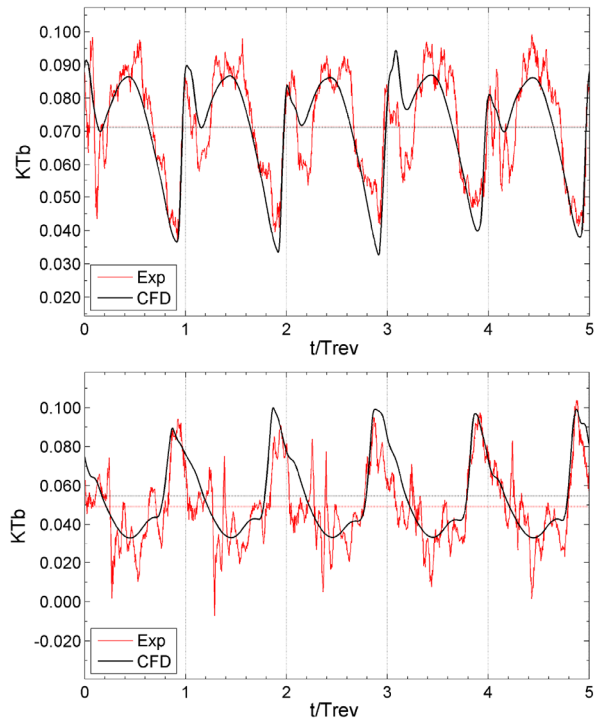


Figure 15. Time histories of blade thrust for heading angles of +35 degrees (top) and -35 degrees (bottom).

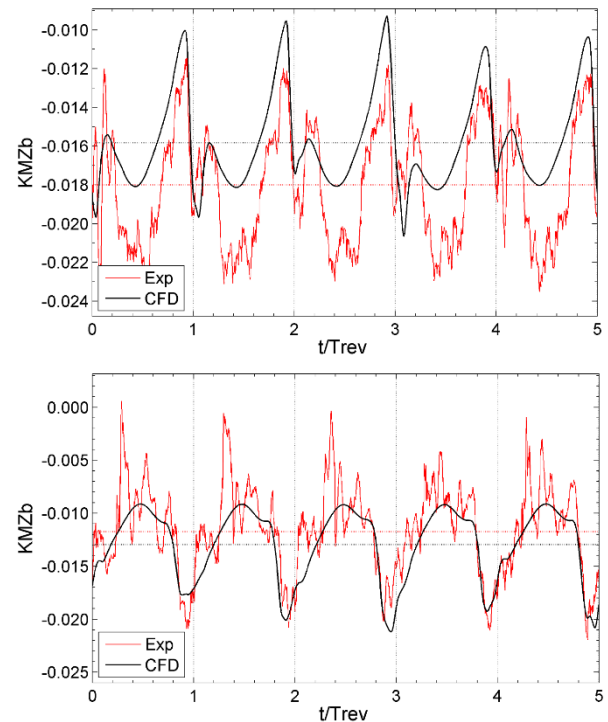


Figure 16. Time histories of bending moment for heading angles of +35 degrees (top) and -35 degrees (bottom).

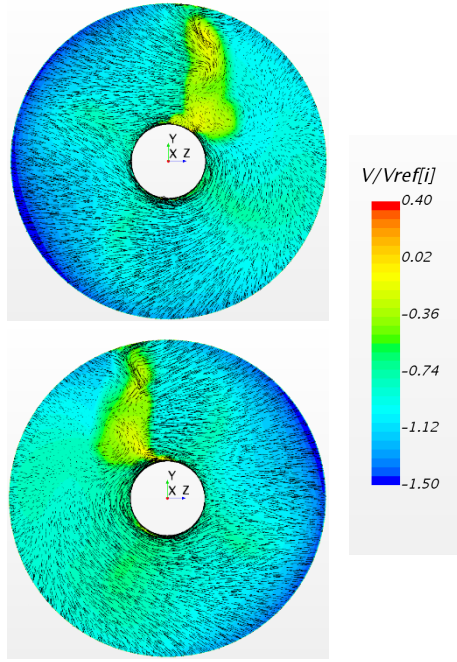


Figure 17. Axial velocity contours and tangential velocity vectors upstream the propeller for the heading angle of +35 degrees (top) and -35 degrees (bottom).

At negative heading angles, the heaviest blade loads due to cross-flow are observed around 12 o'clock position, where they appear reduced by wake induced velocities whose direction is opposite to the cross-flow. In addition to the above, there is also effect of flow retardation in the pod wake, which results in local increase of blade loading once it enters the wake area. However, the effect of flow retardation is comparable at positive and negative headings. Thus, it can be concluded that the major contribution to the unsteadiness of blade loads is related to the interaction of propeller with the separated wake from the pod housing.

5 EFFECT OF FREE-SURFACE

The effect of free surface on the performance of the ducted pushing thruster is investigated in straight flow condition for different magnitudes of immersion. The numerical simulations are run with an initially undisturbed free surface, using the "Flat VOF wave" model implemented in STAR-CCM+. The mesh used in the simulations with free surface was slightly modified compared to the mesh used in previous studies under open water conditions. The general mesh structure and refinement pattern were similar, but the cell count in the propeller mesh block was reduced in favor of more refinement in the vicinity of free surface, both in vertical and horizontal directions, and close to the propeller. The number of cell in the propeller block was about 2.5 million, while the total grid size was

approximately 21.75 million cells. The numerical setup in terms of turbulence model and temporal discretization was kept the same as in the previous calculations. The simulated cases are summarized in Table 5. The immersion of propulsor, H , is defined as the vertical distance from the propeller center to undisturbed free surface level.

Table 5. Simulated conditions with free-surface

Advance coefficient	Immersion [H/D_p]
0.6	2, 1.7, 1.5, 1.3, 1, 0.8, 0.5
0.2	1.5, 1, 0.8

It has been noticed that, at early runtime instances of the simulations with free surface, the air is sucked from the air-water phase interface toward the propulsor even for deep submergences. Only after a sufficiently large number of propeller revolutions the propeller becomes free of the air fraction, and a "stationary" solution for free surface is attained. Figure 18 shows the flow around the propeller at different solution time instances for the immersion of $H/D_p = 1$. After about 20 revolutions, no air fraction and no significant changes in the flow around free surface and propulsor are observed. The first 20 revolutions are thus not included in the estimation of the time-averaged forces.

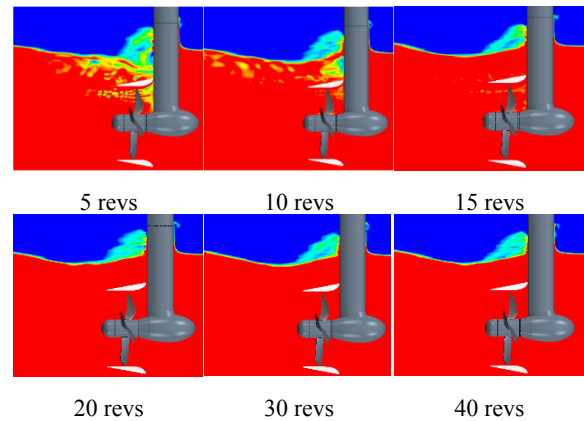


Figure 18. Contours of volume fraction at different solution times for propulsor immersion of $H/D_p=1$ at $J=0.6$.

The variations of propeller thrust and torque, and duct thrust with the magnitude of immersion are illustrated in Figure 19 and Figure 20, respectively. KTP_0 , KTD_0 and KQP_0 refer to the results without free surface at $J=0.6$. Both the propeller thrust and torque remain almost unchanged until $H/D_p=1.3$, and then decrease slightly as the propeller gets closer to the water surface. At very low immersion ($H/D_p=0.5$), a rapid decrease is observed for KTP and KQP . Same observation is made for the duct thrust, but at the immersion of $H/D_p=0.5$, KTD is much more reduced than KTP and KQP , since the upper part of the duct is already out of the water. The analysis of results revealed that, for this loading condition, no ventilation occurs on the

propulsor until the immersion $H/D_p=0.8$, as evident from Figure 21. But at $H/D_p=0.5$, ventilation occurs on the propeller, and a large part of the duct operates continuously in the air (see Figure 22) which, as mentioned, results in a significant reduction of duct thrust.

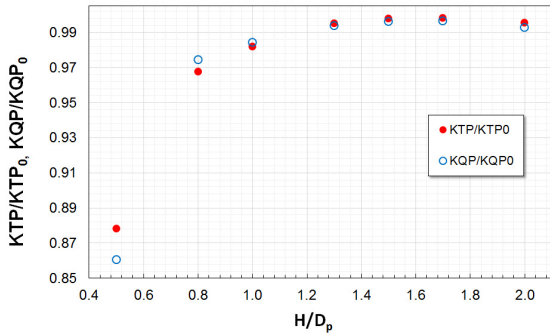


Figure 19. Variation of KTP and KQP with immersion for $J=0.6$.

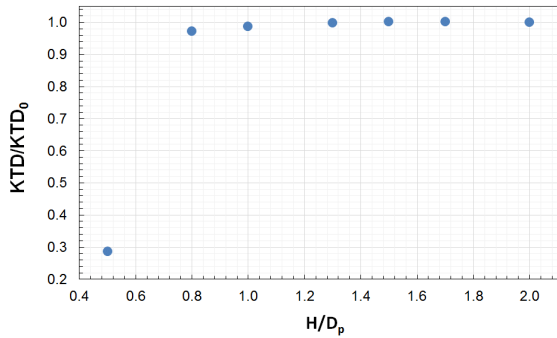


Figure 20. Variation of KTD with immersion for $J=0.6$.

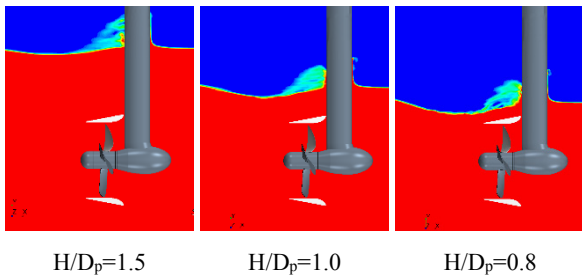


Figure 21. Contours of volume fraction after 40 revolutions for different immersions at $J=0.6$.

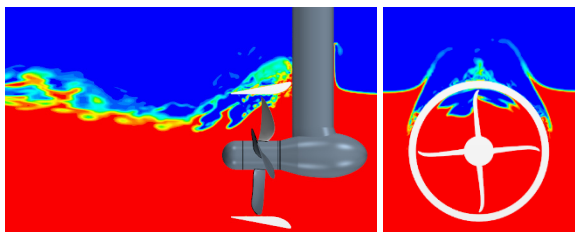


Figure 22. Contours of volume fraction after 40 revolutions at the immersion of $H/D_p=0.5$ at $J=0.6$.

The reduction of KTP, KQP and KTD observed with the decrease of submergence at non-ventilated conditions is attributed to the changes in propeller inflow and flow over the duct. As shown in Figure 23, the inflow upstream of propeller does not change until the immersion of $H/D_p=1.0$, where changes occur close to the propeller hub. They become much more pronounced for $H/D_p=0.8$. In addition, the extent of the wake (in the vertical direction) is reduced resulting in larger velocities. This is supported by the distribution of mean axial velocity at several radial sections on the same plane, as plotted in Figure 24. The main differences appear in the range of $r/R_p < 0.4$ (close to hub) and $r/R_p > 0.8$ (close to blade tip). The aforementioned changes in the propeller inflow are the result of interaction of propulsor with free surface, and they are primarily related to the changes in the wake field generated by the strut. It is observed in Figure 25 that from the immersion of $H/D_p=1.0$ the extent of separated flow region on the strut above the duct is narrower, and the flow velocity is larger.

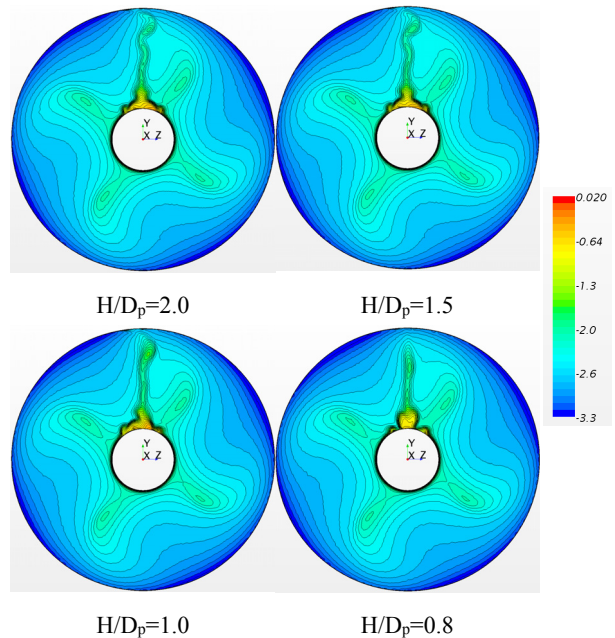


Figure 23. Axial velocity contours upstream of propeller for different immersions at $J=0.6$.

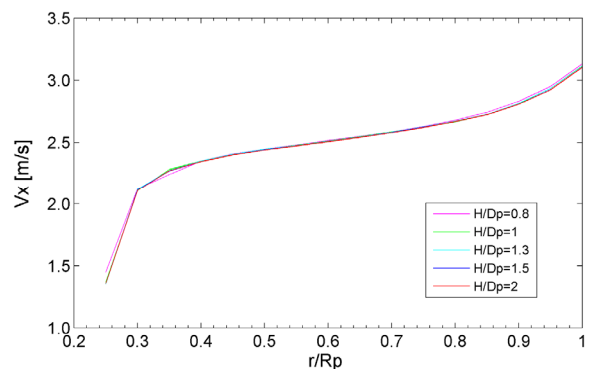


Figure 24. Distribution of mean axial velocity along different radial sections for different immersions at $J=0.6$.

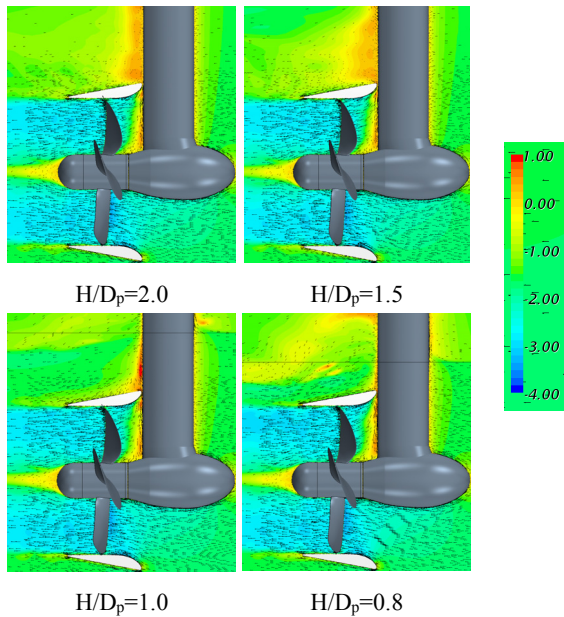


Figure 25. Axial velocity contours and in-plane velocity vectors on a vertical plane at $J=0.6$.

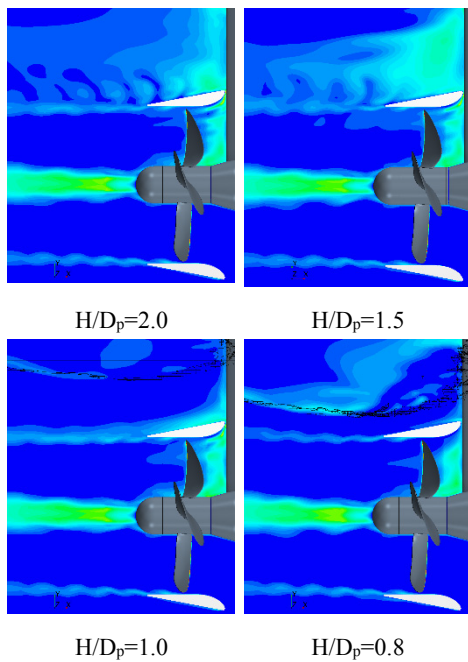


Figure 26. Contours of turbulent kinetic energy (TKE) on a vertical plane at $J=0.6$.

The changes in the extent of the strut wake are also clearly illustrated by the contours of turbulent kinetic energy (TKE), as shown in Figure 26.

Blade forces and moments are also computed for these cases. The results are summarized in Table 6 for some selected immersions. As soon as ventilation occurs on the propeller, the fluctuations of blade forces and moments around their mean values increase significantly.

Table 6. Computed blade forces and moments at $J=0.6$ for different immersions.

Variable	w/o FS	H/D _p =2	H/D _p =1.5	H/D _p =1	H/D _p =0.8	H/D _p =0.5
KT _b	0.062	0.062	0.062	0.061	0.060	0.056
$\sigma(KT_b)$ (%)	5.8	5.5	5.7	5.4	4.5	35.4
10KQ _b	0.079	0.078	0.079	0.078	0.077	0.067
$\sigma(KQ_b)$ (%)	4.1	4.2	4.6	4.3	3.7	34.7
10KMY _b	0.020	0.020	0.020	0.021	0.021	0.000
$\sigma(KMY_b)$ (%)	19.8	20.2	19.9	19.6	17.5	3481.4
10KMZ _b	-0.143	-0.142	-0.143	-0.141	-0.139	-0.120
$\sigma(KMZ_b)$ (%)	4.5	4.0	4.5	4.0	3.0	40.1

For the trawling condition ($J=0.2$), the effect of free surface is more pronounced, as the occurrence of intensive ventilation on propulsor is found already at the immersion of $H/D_p=0.8$ as indicated by Figure 27. At this magnitude of immersion, the air is sucked from the free surface into the propeller through the gap between the strut and duct, and it is then entrained by the blades along the duct interior surface to the bottom part of the duct (see Figure 28). Only a few immersions were investigated for this heavy loading condition. However, Figure 29 shows a significant reduction of propeller thrust, torque and, in particular, duct thrust as the propulsor immersion decrease to $H/D_p=0.8$. The single blade loads given in Table 7 exhibit in general minor variations with immersion, but a significant increase in their oscillations at $H/D_p=0.8$ (seen from larger standard deviations σ) is indicative of the presence of ventilation.

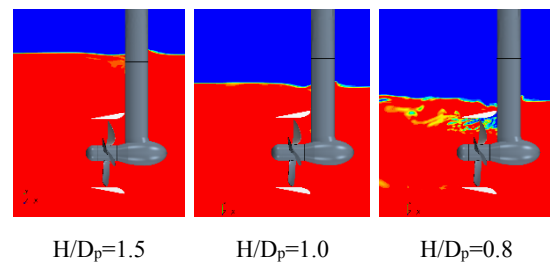


Figure 27. Contours of volume fraction after 40 revolutions for different immersions at $J=0.2$.

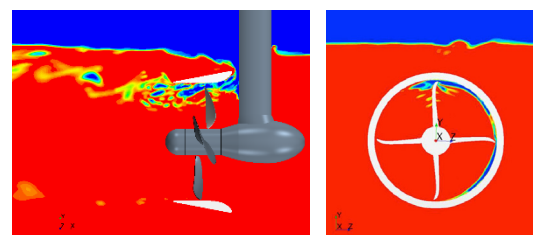


Figure 28. Contours of volume fraction for the immersion of $H/D_p=0.8$ at $J=0.2$.

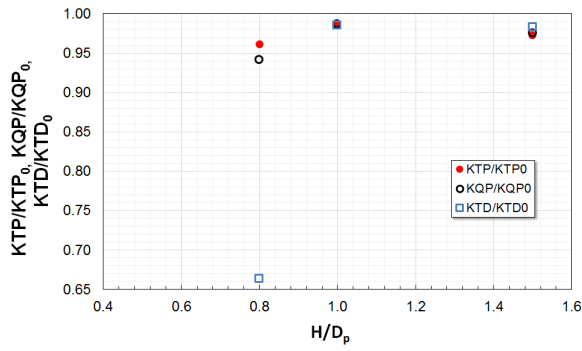


Figure 29. Variation of KTP, KTD and KQP with immersion for J=0.2.

Table 7. Computed blade forces and moments at J=0.2 for different immersions.

Variable	W/o FS	H/Dp=1.5	H/Dp=1	H/Dp=0.8
KTb	0.079	0.077	0.078	0.077
$\sigma(KTb)(\%)$	3.6	3.3	3.6	11.3
10KQb	0.096	0.093	0.095	0.090
$\sigma(KQb)(\%)$	2.8	2.7	3.0	11.2
10KMYb	0.011	0.012	0.012	-0.005
$\sigma(KMYb)(\%)$	25.7	24.9	26.8	203.2
10KMZb	-0.183	-0.179	-0.181	-0.170
$\sigma(KMZb)(\%)$	3.3	2.6	3.0	13.9

6 CONCLUSION

A detailed verification and validation study is prerequisite for numerical simulation of complex flow phenomena associated with dynamic loads on azimuthing propulsors. The results of the present work show that a good agreement can be achieved between the CFD calculations by an unsteady RANS method and experimental data for a ducted pushing thruster operating in straight flow and oblique flow, in the range of relevant loading conditions in the 1st quadrant. The above conclusion stands for both the integral forces and moments on the unit and individual blade loads, including their amplitudes and time histories, with the exception of steering moment, where larger differences are found. The steering moment (excluding duct contribution), as a quantity of smaller order of magnitude compared to other forces and moments acting on the thruster, is very sensitive to small differences in flow pattern, resulting in changes in the locations of the force centers, and hence force arms.

The forces and moments on the ducted azimuth thruster reveal the asymmetry with respect to positive and negative heading angles typical for pushing pod units. The said asymmetry is associated with the interaction of the rotating propeller with the cross-flow in separated wake behind the strut. Due to the flow straightening effect of the duct, the asymmetry of loads acting on the ducted unit is found to be

smaller compared to the case of open pushing thruster. For a unit with right-handed propeller, the loads are smaller at negative heading angles, where the oblique flow on propulsor is from starboard. At the same time, both the calculation results and experimental measurements show that, at negative headings, the amplitudes of single blade loads are larger than at positive headings, except the blade spindle moment, which shows an opposite trend.

The mentioned flow straightening effect of the duct results in relatively small side forces produced by propeller, especially at small heading angles, where the main contributions to the side force and steering moment are those of the duct.

At zero heading, propeller develops a small side force acting in the direction of portside (for right-handed propeller) due to its interaction with the wake of the pod housing. This small side force causes a deviation of the total reaction force and results in a non-zero steering moment acting on the unit. The steering moment is larger at lower J values, where propeller loading is heavier. This phenomenon has direct impact on course-keeping characteristics of vessels equipped with pushing pod propulsors.

The frequency analysis of forces and moments acting on propulsor at large heading angles reveals, in addition to the blade frequency, the presence of a lower frequency peak, which is related to the vortex shedding process that accompanies flow separation on the leeward side of the duct.

The presence of free surface causes important changes in the performance characteristics of the ducted thruster. In free sailing, the influence of free surface becomes appreciable at the relative submergence H/Dp around 0.8, where both the propeller thrust and duct thrust appear reduced to about 3% from their levels in open water conditions, without the occurrence of ventilation. The effect of free surface is more pronounced at heavier loading conditions such as those of trawling, where at Hp/D=0.8 intensive ventilation develops on the duct and propeller, resulting in loss of propeller thrust of 4% and loss of duct thrust of 33-34%. The process of ventilation is associated with air entrainment by propeller blades on the duct interior surface and a very large increase of unsteady blade loads.

ACKNOWLEDGEMENT

The work presented here has been conducted within the frameworks of the ongoing R&D Project "INTER-THRUST" supported by the MARTEC II ERA-NET program (Maritime Technologies). The "INTER-THRUST" consortium members are: SINTEF Ocean (Norway), Hamburg University of Technology (Germany), Voith Turbo Schneider Propulsion GmbH & Co. KG (Germany), Jastram GmbH und Co. KG (Germany), and Havyard Group AS (Norway).

REFERENCES

- Bhattacharyya, A., Krasilnikov, V.I., and Steen, S. (2016), 'Scale Effect on Open Water Characteristics of a Controllable Pitch Propeller working within Different Duct Designs'. Ocean Engineering 112, pp. 226-242.
- Funeno, I. (2009), 'Hydrodynamic Optimal Design of Ducted Azimuth Thrusters'. Proceedings of the SMP'09, Trondheim, Norway.
- Koushan, K. (2006a). 'Dynamics of ventilated propeller blade loading on thrusters due to forced sinusoidal heave motion'. Proceedings of 26th Symposium on Naval Hydrodynamics, Rome, Italy.
- Koushan, K. (2006b), 'Dynamics of propeller blade and duct loadings on ventilated ducted thrusters operating at zero speed'. Proceedings of T-POD06 - 2nd International Conference on Technological Advances in Podded Propulsion, Brest, France.
- Koushan, K., Krasilnikov, V.I. (2008), 'Experimental and Numerical Investigation of Open Thrusters in Oblique Flow Conditions'. Proceedings of 27th Symposium on Naval Hydrodynamics, Seoul, Korea.
- Krasilnikov, V.I., Zhang, Zh. and Hong, F. (2009). 'Analysis of Unsteady Propeller Blade Forces by RANS'. Proceedings of the 1st International Symposium on Marine Propulsors SMP'09, Trondheim, Norway.
- Palm, M., Jürgens, D. and Bendl, D. (2011), 'Numerical and Experimental Study on Ventilation for Azimuth Thrusters and Cycloidal Propellers' Proceedings of the SMP'11, Hamburg, Germany.